

# The dust envelope of the pre-planetary nebula IRAS19475+3119

Geetanjali Sarkar<sup>1</sup> and Raghvendra Sahai<sup>2</sup>

*Department of Physics, Indian Institute of Technology, Kanpur-208016, U.P., India*

*Jet Propulsion Laboratory, MS 183-900, 4800 Oak Grove Drive, Pasadena, CA 91109, U.S.A.*

gsarkar@iitk.ac.in, raghvendra.sahai@jpl.nasa.gov

## ABSTRACT

We present the spectral energy distribution (SED) of the pre-planetary nebula, IRAS 19475+3119 (I 19475), from the optical to the far-infrared. We identify emission features due to crystalline silicates in the ISO SWS spectra of the star. We have fitted the SED of I 19475 using a 1-D radiative transfer code, and find that a shell with inner and outer radii of  $8.8 \times 10^{16}$  and  $4.4 \times 10^{17}$  cm, and dust temperatures ranging from about 94 K to 46 K provide the best fit. The mass of this shell is  $\gtrsim 1 [34 \text{ cm}^2 \text{ g}^{-1} / \kappa(100 \mu\text{m})][\delta/200] M_{\odot}$ , where  $\kappa(100 \mu\text{m})$  is the  $100 \mu\text{m}$  dust mass absorption coefficient (per unit dust mass), and  $\delta$  is the gas-to-dust ratio. In agreement with results from optical imaging and millimeter-wave observations of CO emission of I 19475, our model fits support an  $r^{-3}$  density law for its dust shell, with important implications for the interaction process between the fast collimated post-AGB winds and the dense AGB envelopes which results in the observed shapes of PPNs and PNs. We find that the observed JCMT flux at sub-millimeter wavelengths ( $850 \mu\text{m}$ ) is a factor  $\sim 2$  larger than our model flux, suggesting the presence of large dust grains in the dust shell of I 19475 which are not accounted for by our adopted standard MRN grain size distribution.

*Subject headings:* Stars: Circumstellar Matter, Stars: AGB and post-AGB, Stars: Individual: Alphanumeric: IRAS 19475+3119

## 1. Introduction

Pre-Planetary nebulae (PPNs), objects in transition between the AGB and planetary nebula (PN) evolutionary phases, hold the key to our understanding of the relationship between these late evolutionary stages of low and intermediate mass ( $\sim 1 - 8 M_{\odot}$ ) stars.

The hydrodynamic interaction of one or more fast, collimated post-AGB outflows, believed to occur during the PPN phase, with the dense, massive, slowly-expanding spherical AGB wind is believed to be responsible for shaping planetary nebulae (Sahai & Trauger 1998, Sahai 2002). Imaging surveys with the Hubble Space Telescope have been crucial in revealing a wide variety of aspherical morphologies in PPNs (e.g. Sahai 2004; Ueta et al. 2000), however the bulk of the circumstellar mass, which often resides in a spherical, dusty component surrounding the central aspherical nebula, is not well-probed in these data. Thus a crucial ingredient for theoretical studies of such interactions, namely the mass and density of the ambient circumstellar medium (e.g., Lee & Sahai 2003, 2004), is lacking for a majority of the PPNs discovered in HST surveys. Although attempts have been made to estimate the mass from submillimeter data (e.g. Gledhill et al. 2002), these are compromised by the simplifying assumptions about the dust temperature.

The mineralogy of circumstellar dust shells around PPNs became possible with the wavelength coverage and spectral resolution offered by the Infrared Space Observatory (ISO) (see e.g. Hrivnak et al. 2000; Molster et al. 2002a, b, c; Gauba & Parthasarathy 2004 and references therein). In order to understand the grain temperatures, mass-loss history and morphology responsible for the formation of these minerals in the circumstellar environment of PPNs, detailed modelling of the spectral energy distributions (SEDs) of a few PPNs (e.g., HD161796, Hoogzaad et al. 2002; IRAS 16342-3814, Dijkstra et al. 2003a; IRAS 16279-4757, Matsuura et al. 2004; Gauba & Parthasarathy 2004) have been undertaken.

In this paper, we examine the composition and distribution of dust in the PPN, IRAS 19475+3119 (hereafter I19475) and model its SED from the optical to the far-infrared to set constraints on the physical properties of its dust shell (mass, temperature, size). I19475 is listed as a F3Ia star in the Case-Hamburg luminous stars survey (Stock et al. 1960). High resolution optical spectra of the star have confirmed its post-AGB nature (Klochko et al. 2002; Sivarani et al. 2001; Arellano Ferro et al. 2001). A point-symmetric nebula with an extent of  $4.9'' \times 3.4''$  has been seen in J-band polarized flux images (Gledhill et al. 2001). CO J=1–0 and 2–1 emission typical of AGB and post-AGB objects was detected from the circumstellar envelope of the star (Loup et al. 1993). Hrivnak & Bieging (2005) noticed asymmetry and possible structure in the CO J=2–1 and 4–3 lines. Recent imaging of I19475 with the Hubble Space Telescope at optical wavelengths reveals a dusty quadrupolar nebula and spherical halo, surrounding the central star (Sahai 2004; Sahai et al. 2006).

The rest of the paper is organized as follows. In §2, we provide observational details of the ISO data, in §3 we describe the ISO spectra, and the re-construction of I19475’s spectral energy distribution (SED) from these as well as broad-band photometric data, in §4 we describe our modelling of the SED using a spherical dust radiative transfer code, in

§ 5 we discuss our models, and in § 6, we present our conclusions.

## 2. ISO Observations

Infrared Space Observatory (ISO) observations of I 19475 were extracted from the ISO data archive. These include spectroscopic observations made with the Short Wavelength Spectrometer (SWS) and the Long Wavelength Spectrometer (LWS) and spectrophotometric observations made with the imaging photopolarimeter (ISOPHOT) onboard ISO. An off-source measurement made with the LWS in order to estimate the background was also extracted from the archive. A log of the observations is given in Table 1.

ISO SWS spectra have a wavelength coverage of 2.38–45.2  $\mu\text{m}$ . Our spectra were obtained in the low resolution mode (AOT 01) of the SWS instrument (de Graauw et al. 1996) with a  $33'' \times 20''$  aperture. Each SWS spectrum contains 12 subspectra, that each consist of two scans, one in the direction of decreasing wavelength (‘up’ scan) and the other in the direction of increasing wavelength (‘down’ scan). There are small regions of overlap in wavelength between the sub-spectra. Each sub-spectrum is recorded by 12 independent detectors.

LWS spectra extend from 43–197  $\mu\text{m}$ . The LWS observations were obtained in LWS01 mode, covering the full spectral range at a resolution ( $\lambda/\Delta\lambda$ ) of  $\sim 200$ . The LWS circular field of view had a diameter of  $84''$ . The ISO LWS instrument and its calibration are described in Clegg et al. (1996) and in Swinyard et al. (1996) respectively.

ISOPHOT observations were carried out using the spectrophotometer subsystem PHT-S. PHT-S consists of two low-resolution grating spectrometers covering the wavelength ranges 2.5–4.9  $\mu\text{m}$  (PHT-SS) and 5.8–11.6  $\mu\text{m}$  (PHT-SL) and having a common entrance aperture of  $24'' \times 24''$ . Each channel has a linear 64-element array of Si:Ga detectors. The spectral band width (FWHM) of a single detector is 0.0383  $\mu\text{m}$  for PHT-SS and 0.0918  $\mu\text{m}$  for PHT-SL, resulting in a mean  $\lambda/\Delta\lambda$  of about 95 for both channels. A more detailed description of PHT-S has been given by Klaas et al. (1997). In the PHT40 observing mode spectrophotometry is performed simultaneously at wavelengths 2.5–4.9  $\mu\text{m}$  and 5.8–11.6  $\mu\text{m}$ .

Table 1: Log of ISO observations

Object	Instrument	Date of Obs.	Duration of Obs. (s)	TDT <sup>a</sup>	Mode <sup>b</sup>	Speed <sup>c</sup>
IRAS 19475+3119	SWS	12/11/1996	1140	36100905	SWS01	1
IRAS 19475+3119	SWS	19/04/1997	6538	52000931	SWS01	4
IRAS 19475+3119	LWS	12/11/1996	1266	36100904	LWS01	–
Off-source	LWS	12/11/1996	1268	36100943	LWS01	–
IRAS 19475+3119	PHT-S	19/04/1997	364	52000932	PHT40	–

<sup>a</sup>TDT number uniquely identifies each ISO observation. <sup>b</sup>Observing mode used. <sup>c</sup>Speed corresponds to the scan speed of observation.

### 3. Analysis

Details of data reduction are described in Appendix A. The reduced SWS, LWS, and PHT-S spectra are shown in Figs.1, 2 & 3 , respectively.

#### 3.1. Infrared spectral features

Emission features at  $33.6\ \mu\text{m}$  and  $43\ \mu\text{m}$  were observed in the SWS spectra (Fig.1). The  $33.6\ \mu\text{m}$  feature is attributed to forsterite, a crystalline silicate (Waters et al. 1996; Waters & Molster 1999; Gauba & Parthasarathy 2004). Both pyroxenes (such as enstatite) and water-ice show features at  $\sim 43\ \mu\text{m}$ . ISO observations of post-AGB stars have shown that the  $43\ \mu\text{m}$  feature is almost always accompanied with a prominent emission feature at  $40.5\ \mu\text{m}$  attributed to pyroxenes such as enstatite and/or diopside (Molster et al. 2002b). The non-detection of the  $40.5\ \mu\text{m}$  feature in I19475 is therefore puzzling, suggesting that pyroxenes are not (or only very weakly) present in this object

The only other post-AGB object which shows a spectrum in the  $\sim 40\ \mu\text{m}$  region similar to that of I19475, is HD161796 (Molster et al. 2002b), which, like I19475, is a high latitude F3Ib post-AGB star with a detached circumstellar dust envelope (Parthasarathy & Pottasch 1986; Hoogzaad et al. 2002). HD161796 shows a prominent  $43\ \mu\text{m}$  feature and a weak  $40.5\ \mu\text{m}$  feature – in order to fit these features, Molster et al. (2002c) need a combination of pyroxenes and crystalline water ice, with the latter dominating the  $\sim 40\ \mu\text{m}$  emission complex. This is because in the  $\sim 40\ \mu\text{m}$  region, crystalline water ice contributes a feature only at  $43\ \mu\text{m}$ , hence its dominant presence helps to reduce the intensity of the  $40.5\ \mu\text{m}$  feature (produced by pyroxene only) relative to the  $43\ \mu\text{m}$  one (produced by pyroxene and ice). The presence of crystalline water ice in HD161796 is supported by the prominent  $62\ \mu\text{m}$  feature in its LWS spectrum.

Similarly, if the  $43\ \mu\text{m}$  feature in I19475 is due to (or dominated by) crystalline water ice, then one would expect to see a crystalline water-ice feature at  $\sim 62\ \mu\text{m}$ . We now examine the possibility that the latter is not seen because it may be much weaker compared to the  $43\ \mu\text{m}$  feature if the ice mantles are deposited onto the dust grains at a temperature above 110K (Smith et al. 1994), by as much as a factor of 3.1. And in fact, in most PPNs, the continuum-subtracted peak intensity of the  $62\ \mu\text{m}$  crystalline water-ice feature when present, is about a factor of  $\sim 3$  lower than the  $43\ \mu\text{m}$  feature (see e.g. Molster et al. 2002c). The continuum-subtracted peak intensity of the  $43\ \mu\text{m}$  feature in our spectra is  $14.4 \pm 1.4\ \text{Jy}$  (SWS 36100905) and  $17.6 \pm 0.8\ \text{Jy}$  (SWS 52000931) respectively. Hence we would expect the  $\sim 62\ \mu\text{m}$  feature in I19475 to have a peak intensity of about 4.6 Jy; given that the

expected width of this feature, both from laboratory and astronomical spectra, is quite large (about  $8\ \mu\text{m}$ ) this feature should have been detected in our spectra. We conclude that the  $62\ \mu\text{m}$  feature is probably not present in I 19475; the identification of the  $43\ \mu\text{m}$  emission feature in our spectra as due to crystalline water ice is thus inconclusive.

Unlike crystalline water ice, amorphous water ice produces a single broad feature with a peak at  $\sim 46\ \mu\text{m}$  (Smith et al. 1994). Molster et al. (2002c) suggest that some amorphous water ice may be present in HD161796 in order to explain modest discrepancies between their model and the data in the  $\sim 40\ \mu\text{m}$  wavelength region. However, in I 19475, the  $43\ \mu\text{m}$  feature is relatively narrow, with a peak at  $42.9 \pm 0.04\ \mu\text{m}$ . The sharpness of this feature suggests that it is unlikely that amorphous water ice has a substantial presence in I 19475. However, without detailed modelling of this feature a small contribution from amorphous water ice cannot be ruled out. This is because even if we assume that all ice condenses in crystalline form (requiring extreme conditions in the AGB outflow), UV radiation from the interstellar medium (ISM) can begin to amorphize the ice (Dijkstra et al. 2003b and references therein).

In the averaged SWS spectrum (Fig. 1c), a weak emission feature at  $\sim 23\ \mu\text{m}$  attributed to crystalline silicates (Molster et al. 2002b) becomes obvious. An emission feature at  $48\ \mu\text{m}$  was detected in the LWS spectrum of I 19475 (Fig. 2). The  $48\ \mu\text{m}$  feature has been observed in several stars (see e.g. Molster et al., 2002b). Ferrarotti et al. (2000) identified this feature with FeSi. However, this identification remains unconvincing since the formation of FeSi would require an environment where  $\text{C/O} \sim 1$ , whereas the  $48\ \mu\text{m}$  feature has been observed in several O-rich stars as well (Molster et al. 2002b). Furthermore, it is as yet not clear if this spectral feature is an artifact in the LWS instrument spectral response function, or a real feature (T. Lim, private communication 2006).

The presence of [CII] emission at  $158\ \mu\text{m}$  in both the on-source and off-source spectra, combined with the absence of [OI] at  $63\ \mu\text{m}$  in the on-source LWS spectrum (Fig. 2) suggests that the [CII] emission can be attributed entirely to contamination from the ISM (see e.g. Castro-Carrizo et al. 2001).

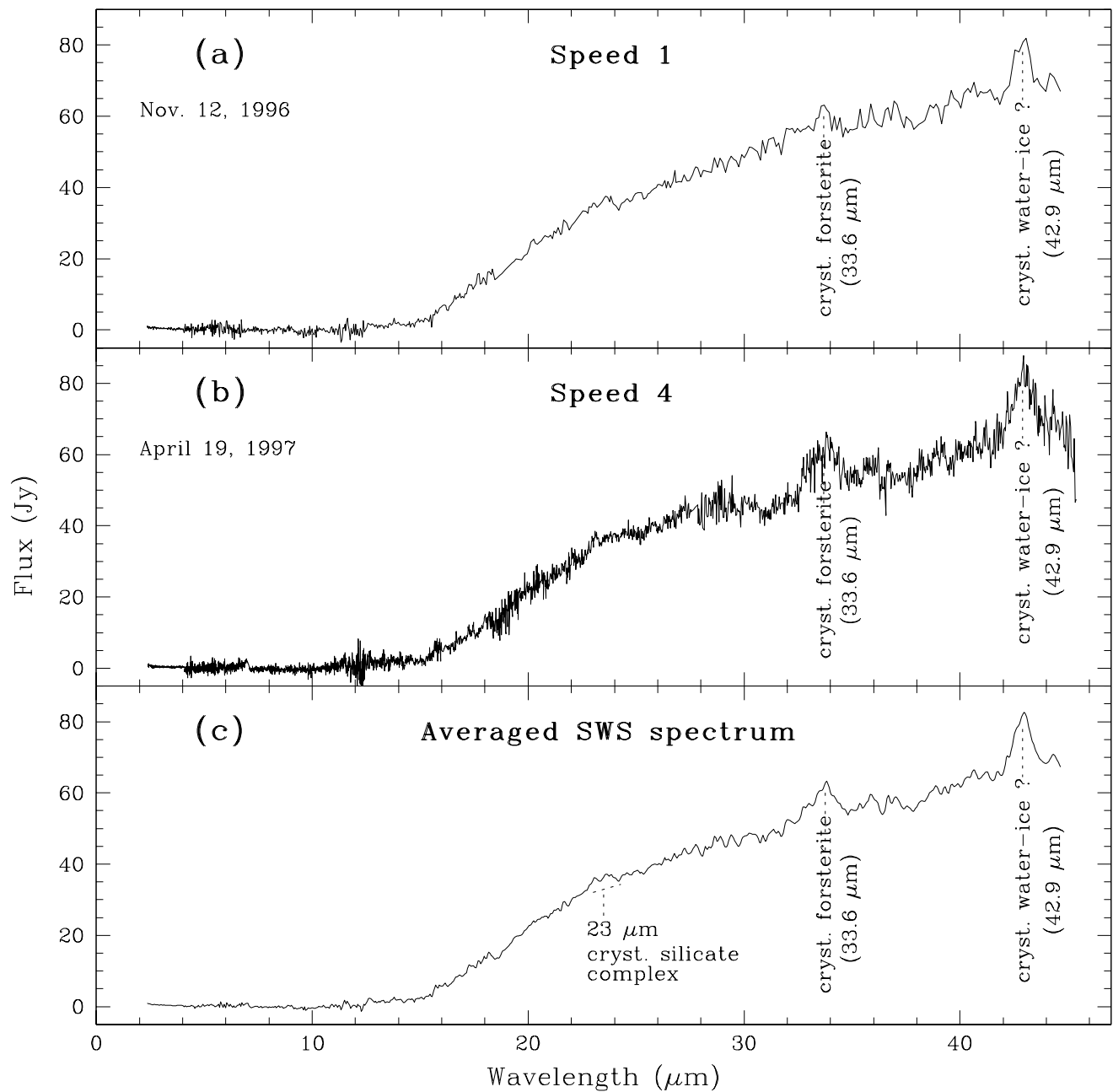


Fig. 1.— SWS spectra of I 19475 taken with (a) Speed 1 and (b) Speed 4 and (c) the averaged SWS spectrum of the star.

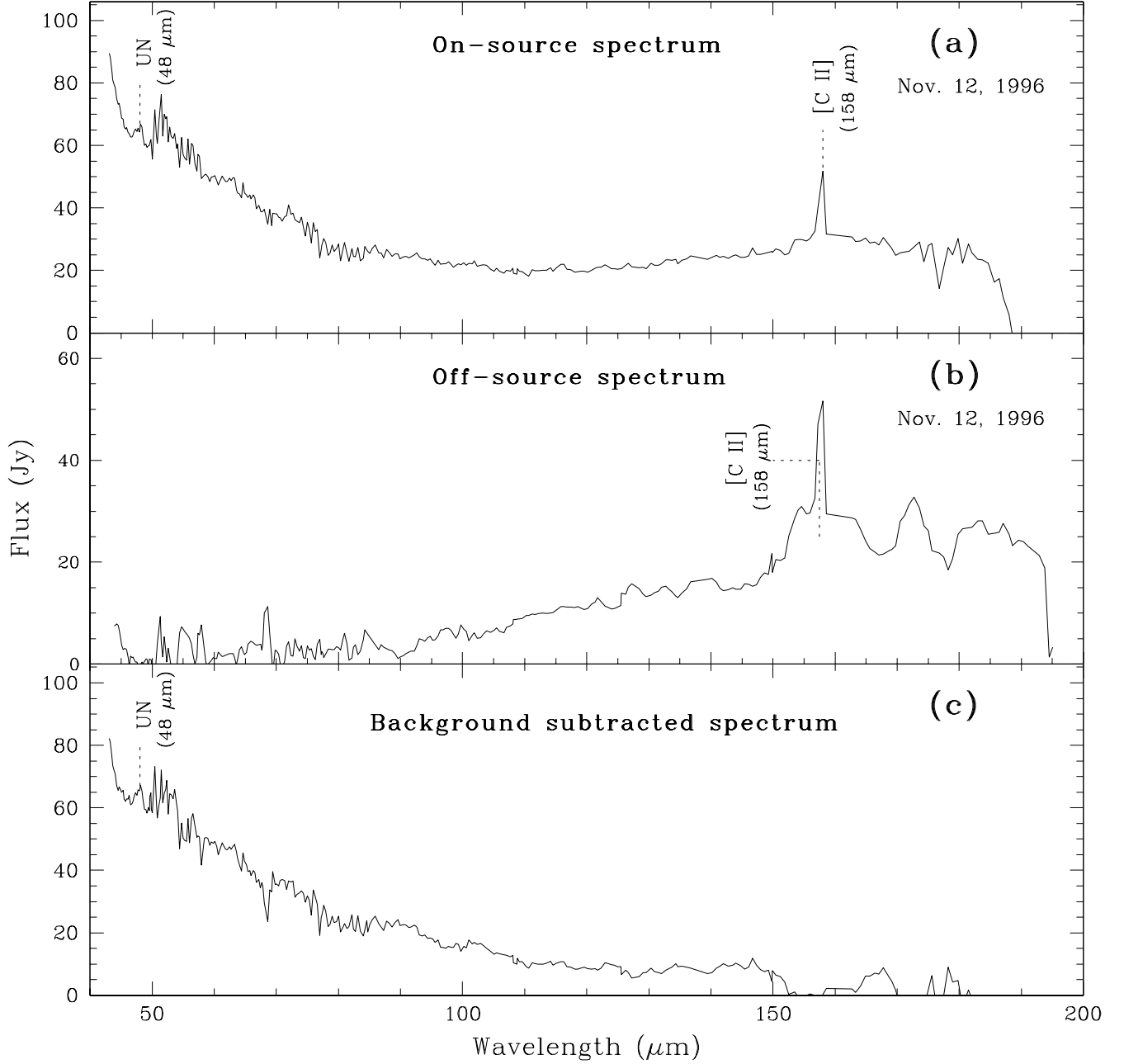


Fig. 2.— (a) The observed LWS spectrum of I 19475, (b) off-source spectrum, and (c) source spectrum after subtraction of the off-source data. The 48  $\mu\text{m}$  emission feature seen in the LWS spectrum is as yet unidentified (UN)



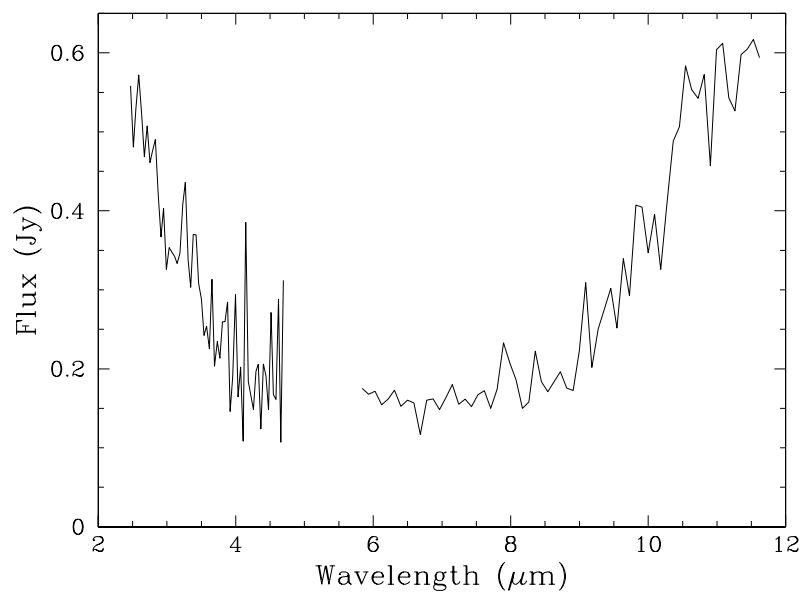


Fig. 3.— The PHT-S spectrum of I19475 recorded with the low resolution grating spectrometers PHT-SS ( $2.5 - 4.9 \mu\text{m}$ ) and PHT-SL ( $5.8 - 11.6 \mu\text{m}$ ) onboard ISO.

### 3.2. Spectral energy distribution (SED)

Both SWS spectra of I 19475 show similar flux distributions (Figs. 1a and b). Therefore, for further analysis, the two SWS observations were averaged together after rebinning the Speed 4 data to the resolution of the Speed 1 SWS data (Fig. 1c). The averaged SWS data were combined with the PHT-S data (Fig. 3) and the background subtracted LWS spectrum of the star (Fig. 2c). The SWS and LWS data showed good agreement in the overlap region. The SWS data below  $14\ \mu\text{m}$  and the LWS data beyond  $143\ \mu\text{m}$  are noisy (see Appendix A and Fig. 2c) and were excluded from further analysis. To reconstruct the SED, the ISO data were combined with the available U,B,V (Reed 2001), R,I (Monet et al. 2003), J,H,K (2Micron All Sky Survey (2MASS); García-Lario et al. 1997) magnitudes, MSX (Midcourse Space Experiment) fluxes and IRAS (Infrared Astronomical Satellite) fluxes of the star (Tables 2, 3 and 4). Color-corrected IRAS fluxes (Table 4) were estimated using the IRAS Explanatory Supplement. We also retrieved the IRAS low resolution spectrum (LRS) from the University of Calgary database ([http://www.iras.ucalgary.ca/~volk/getlrs\\_plot.html](http://www.iras.ucalgary.ca/~volk/getlrs_plot.html)) using the “corrected raw text” option which applies the absolute calibration corrections from Cohen et al. (1992) to the raw IRAS LRS data. The short-wavelength ( $7.7\text{--}13.4\ \mu\text{m}$ ) section of the LRS spectrum is very noisy, and has not been included. The full optical-to-far-infrared SED of the star is shown in Fig. 4.

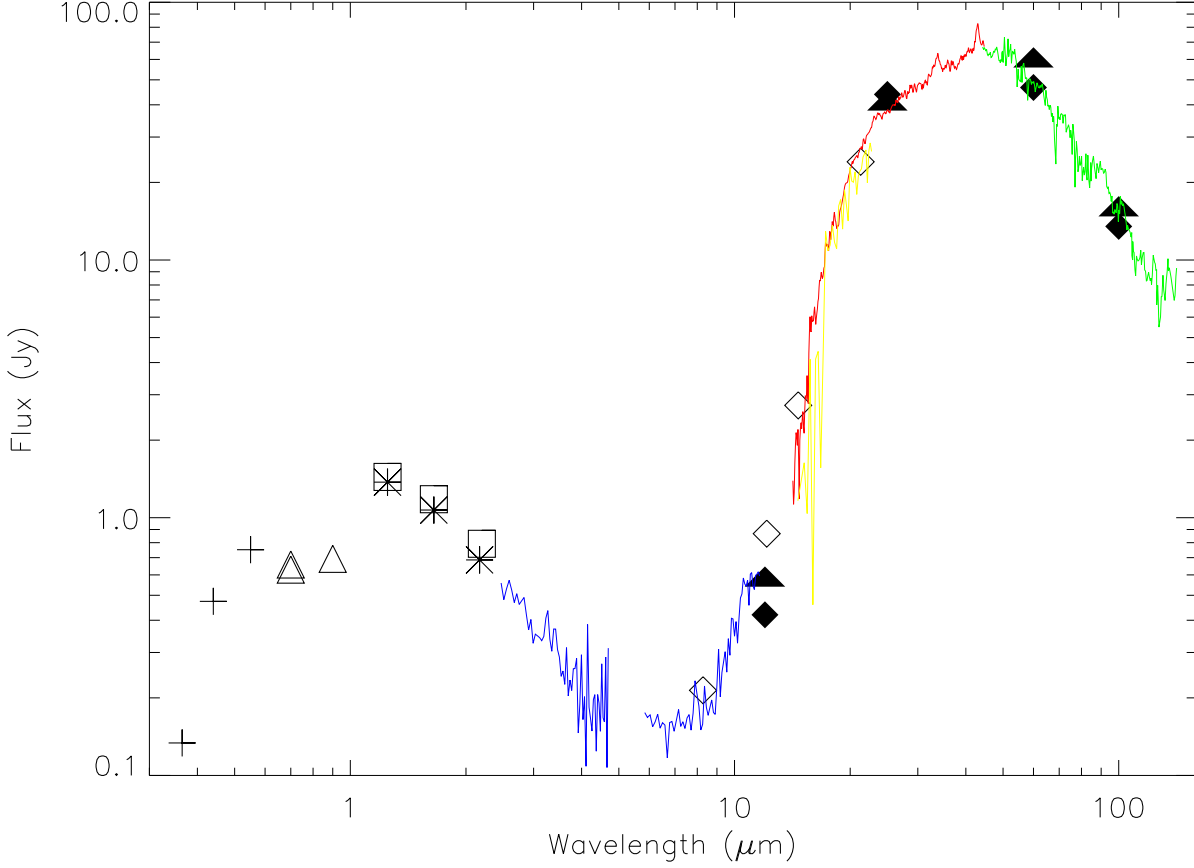


Fig. 4.— The observed SED of I 19475. The plotted data are not corrected for interstellar and circumstellar reddening. U, B, V (plus symbols), R, I (triangles) fluxes are plotted along with J, H, K fluxes (open squares: data from García-Lario et al., 1997; asterisk: 2MASS data), MSX (diamonds) and IRAS data (filled triangles : IRAS fluxes from the Point Source Catalog; filled diamonds : color-corrected IRAS fluxes). Colors highlight the PHT-S (blue), IRAS LRS (yellow), SWS (red) and LWS (green) data.

Table 2: Photometric data of I 19475

U	B	V	R	I	J	H	K
mag	mag	mag	mag	mag	mag	mag	mag
10.404	9.97	9.312	9.14 <sup>a</sup>	8.78	7.73 <sup>c</sup>	7.41 <sup>c</sup>	7.25 <sup>c</sup>
			9.10 <sup>b</sup>		7.773 <sup>d</sup>	7.493 <sup>d</sup>	7.366 <sup>d</sup>

a and b are R-band observations at epochs 1 and 2 respectively (Monet et al., 2003). <sup>c</sup>:García-Lario et al. (1997); <sup>d</sup>: 2MASS data

Table 3: MSX data

MSX fluxes in Janskys			
Band A	Band C	Band D	Band E
8.28 $\mu\text{m}$	12.13 $\mu\text{m}$	14.65 $\mu\text{m}$	21.34 $\mu\text{m}$
0.214	0.867	2.728	24.041

Table 4: IRAS data

IRAS fluxes in Janskys			
12 $\mu\text{m}$	25 $\mu\text{m}$	60 $\mu\text{m}$	100 $\mu\text{m}$
0.54	37.99	55.83	14.76
0.42 <sup>†</sup>	43.9 <sup>†</sup>	46.7 <sup>†</sup>	13.5 <sup>†</sup>

<sup>†</sup>: Color-corrected IRAS fluxes

## 4. Dust Shell Modelling of the SED

We now describe detailed modelling of the SED of I19475, using the 1-D radiative transfer code, DUSTY (Ivezić et al. 1999). DUSTY assumes a spherical geometry and supports various analytical forms for the dust density distribution. The input parameters required for the DUSTY code are the dust temperature on the inner shell boundary ( $T_d$ ), the relative shell thickness ( $Y$  = ratio of the outer to the inner shell radius), the optical depth ( $\tau$ ) at a specified wavelength, the dust grain composition and grain size distribution, and the spectrum of the heating radiation from the central source.

### 4.1. Distance estimates

Although the distance to the source is not a required input for DUSTY, we need it in order to determine the physical size and total mass of the dust shell. Various distance estimates for I19475 are available in literature. Likkell et al. (1987) used a kinematic distance estimate of 6 kpc. Omont et al. (1993) adopted a luminosity of  $10^4 L_\odot$  and estimated a distance of 4.8 kpc. Hrivnak & Bieging (2005) estimated a distance of 4.9 kpc to the object, assuming a luminosity of  $8300 L_\odot$ , appropriate for a core mass of  $0.63 M_\odot$  (Blocker 1995) – we have adopted their values for the models discussed in this paper.

### 4.2. Reddening

The total extinction towards the star, ( $E(B-V)=0.41$ ), was estimated from the difference between the observed  $B-V$  ( $= 0.66$ ) value and intrinsic  $B-V$  ( $(B-V)_O$ ) value for the optical spectral type (F3Ia) of the star. For  $(B-V)_O$  we used a value of  $+0.25$  after interpolating between  $(B-V)_O$  for a F2Ia and a F5Ia star (Schmidt-Kaler 1982). Thus,  $A_V=1.3$ , using  $R_V = 3.1$ , where,  $R_V = A_V/E(B-V)$  (Rieke & Lebofsky 1985). Alternatively, using the numerical algorithm provided by Hakkila et al. (1997), which computes the 3-dimensional visual interstellar extinction and its error from inputs of Galactic longitude and latitude, and distance, from a synthesis of several published studies, we find an interstellar extinction of  $A_V = 1.5 \pm 0.5$ . However, at the low galactic latitude ( $b = +2.73$ ) of the star, galactic extinction maps (e.g. Schlegel et al. 1998) do not provide very reliable estimates of the interstellar extinction. We have corrected the observed optical and near-infrared magnitudes for an extinction  $A_V=1.3$ , using the standard extinction laws by Rieke & Lebofsky (1985).

### 4.3. Stellar model atmosphere parameters

A Kurucz model atmosphere was used as the input stellar spectrum. Several estimates for the effective temperature ( $T_{\text{eff}}$ ) and gravity ( $\log g$ ) of I 19475 are found in literature:  $T_{\text{eff}} = 7200$  K,  $\log g = 0.5$  (Klochko et al. 2002),  $T_{\text{eff}} = 7750$  K,  $\log g = 1.0$  (Arellano Ferro et al. 2001) and  $T_{\text{eff}} = 7500$  K,  $\log g = 0.5$  (Sivarani et al. 2001). In this paper, for the purpose of modelling the SED, we adopted a Kurucz model atmosphere with  $T_{\text{eff}} = 7500$  K and  $\log g = 1.0$ .

### 4.4. Model Fits

In the sections below we discuss the various model fits to the observed data. The input and output parameters corresponding to these models are listed in Table 5.

The modelled flux density (reddened due to circumstellar dust) is scaled to match the observed flux density in the K-band ( $2.2 \mu\text{m}$ ) (García-Lario et al. 1997), corrected for the total (interstellar and circumstellar) extinction. García-Lario et al.’s measurement is consistent, within observational uncertainties, with the 2MASS K-band photometry which is fainter by 0.11 magnitudes. The total extinction at the K-band was estimated to be 0.14 magnitudes. For our best fit DUSTY model (discussed later), the circumstellar extinction at the K-band (in optical depth units) is 0.04.

We have chosen to use the  $2.2 \mu\text{m}$  flux rather than, e.g., an optical flux, for scaling the model to the data, in order to minimise the sensitivity of our results to the following two modelling uncertainties. First, we do not have a very reliable estimate for the interstellar extinction, and second, we are using a 1-D model for an object where a significant part of the scattered light contribution at short wavelengths comes from non-spherical components. At  $2.2 \mu\text{m}$ , the wavelength is (i) sufficiently long that the scattered light contribution is small compared to the direct (but extincted) stellar contribution, and the (uncertain) extinction correction is small, and is (ii) sufficiently short, that the dust shell does not contribute significantly via emission (so our scaling is not affected by the dust properties which are to be derived from the model fitting).

#### 4.4.1. Grain types and size distribution

We have selected grain types for our models from the six different grain types whose constants are directly available in DUSTY: “warm” (Sil-Ow) and “cold” (Sil-Oc) silicates

from Ossenkopf et al. (1992), silicates and graphites (Sil-DL and grf-DL) from Draine and Lee (1984), amorphous carbon (amC-Hn) from Hanner (1988) and SiC (SiC-Pg) from Pégourié (1988). We find that using silicate grains (Sil-Ow, Sil-Oc, Sil-DL) provide good fits to the SED. The use of silicate grains is also supported by our discovery of silicate features (crystalline forsterite and pyroxenes) in the SWS spectrum of I19475 (Fig. 1). Fig. 5 shows the modelled fits to the observed SED using Sil-Ow, Sil-Oc and Sil-DL grains. Optical constants of the Sil-DL grains from Draine and Lee (1984) are based on a combination of laboratory measurements and astronomical observations. Optical constants of the warm oxygen-deficient (Sil-Ow) and cool oxygen-rich (Sil-Oc) silicates are based on observational determinations of the opacities of circumstellar and interstellar silicates as well as laboratory data (Ossenkopf et al. 1992). In estimating the optical constants of Sil-Ow and Sil-Oc, the effects of small spherical inclusions of various materials (oxides, sulfides, carbides, amorphous carbon and metallic iron) upon silicate opacities were taken into account. Fig. 5 shows that using Sil-Oc has the effect of producing slightly higher flux at  $\sim 18 - 25\mu\text{m}$ . Sil-Ow grains appear to provide the best possible fit to the SED from the near to the far-infrared. We therefore adopted Sil-Ow for the purpose of modelling.

The standard Mathis, Rumpl, Nordsieck (MRN) (Mathis et al. 1977) power law was assumed for the grain size distribution, i.e.,  $n(a) \propto a^{-q}$  for  $a_{\min} \leq a_{\max}$  with  $q = 3.5$ ,  $a_{\min} = 0.005 \mu\text{m}$  and  $a_{\max} = 0.25 \mu\text{m}$ .

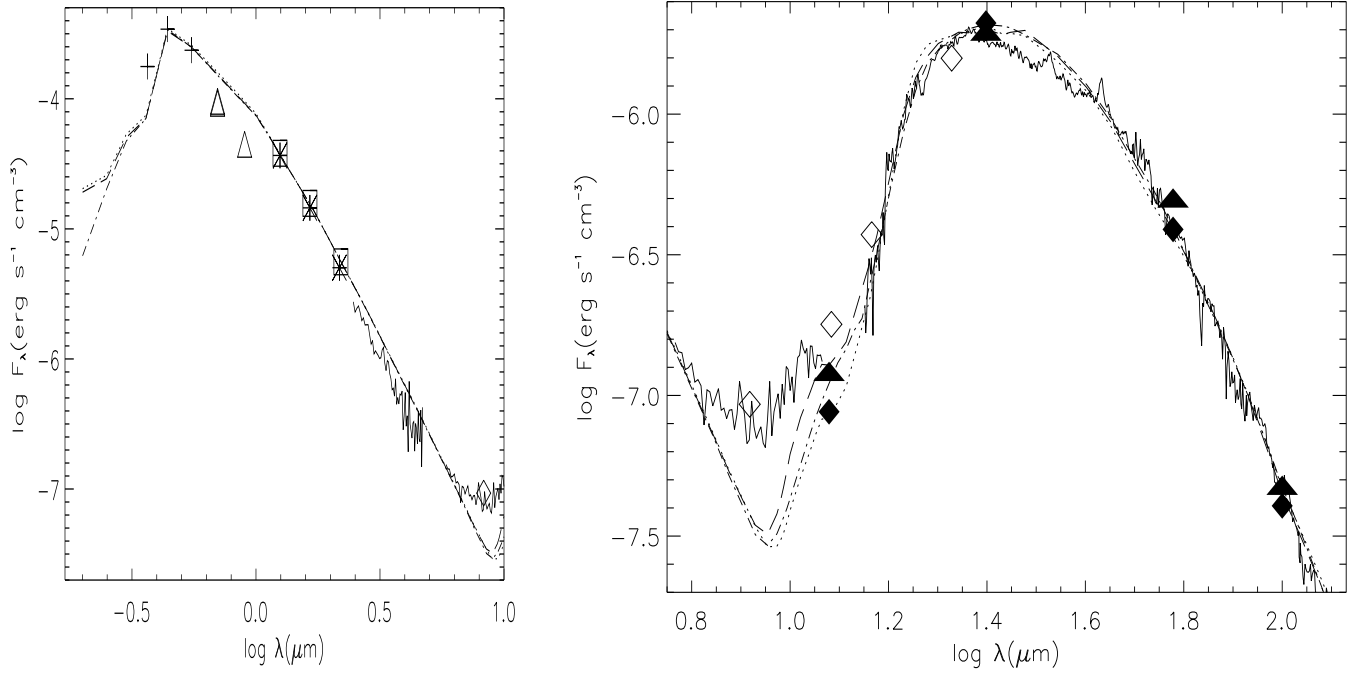


Fig. 5.— Model fits to the observed SED using Sil-Ow (dashed curve), Sil-Oc (dotted curve) and Sil-DL (dashed-dotted curve) grain types (model numbers 1, 2 and 3 in Table 5). The meanings of the symbols are as in Fig. 4. The PHT-S, SWS and LWS spectra are shown as solid curves.



#### 4.4.2. *Density distribution*

We tried two power laws,  $r^{-2}$  and  $r^{-3}$ , for the density distribution. The best fits in the case of the  $r^{-2}$  power law for  $Y$  of 5, 10 and 15 are shown in Fig. 6. Using the  $r^{-2}$  power law, we find that even with  $Y$  as small as 5, the modelled flux systematically exceeds the LWS flux beyond  $\sim 70 \mu\text{m}$ . Adopting an  $r^{-3}$  density distribution and  $Y = 5$ , produces a good fit to the SED upto the limit of the LWS spectrum. For  $Y > 5$ , the modelled flux again begins to exceed the observed LWS flux beyond  $100 \mu\text{m}$ . The best fit models using  $r^{-3}$  power law and  $Y = 5$  and 15 are shown in Fig. 7.

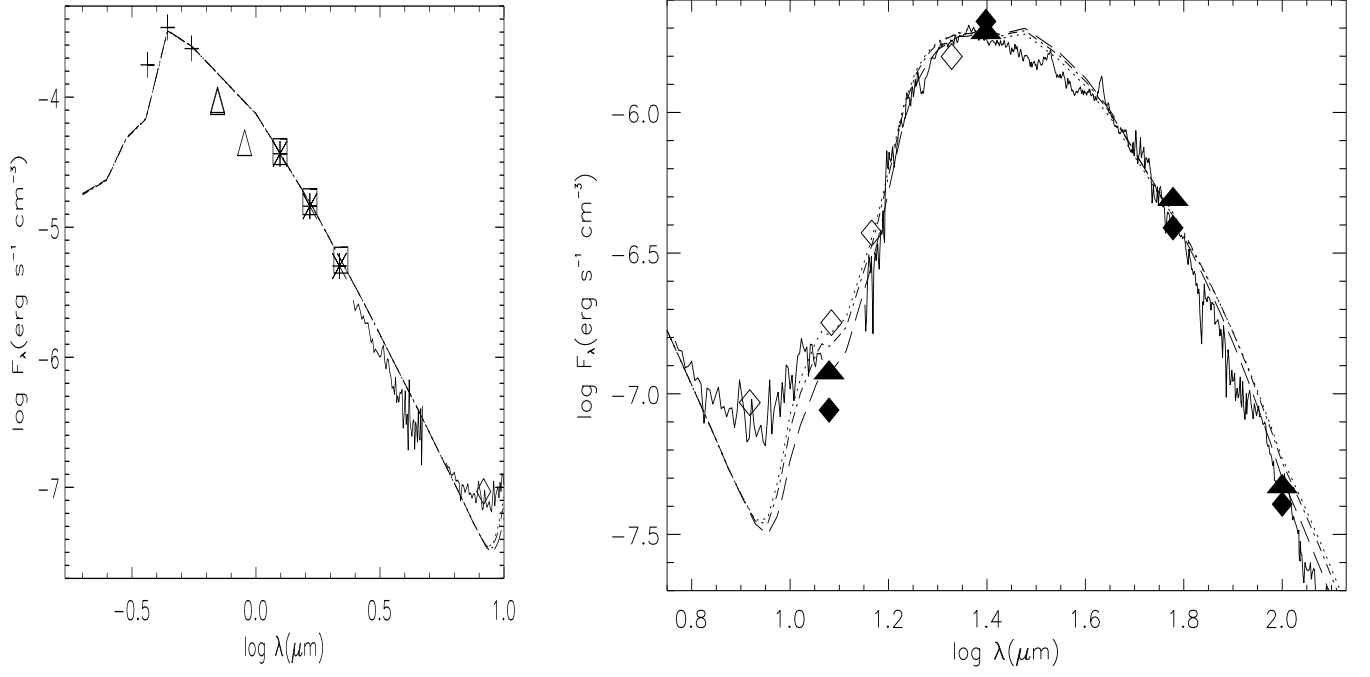


Fig. 6.— As in Fig. 5, but showing model fits using a  $r^{-2}$  density distribution and relative shell thickness of 5 (dashed line), 10 (dashed-dotted) and 15 (dotted) (model numbers 4, 5 and 6 in Table 5).

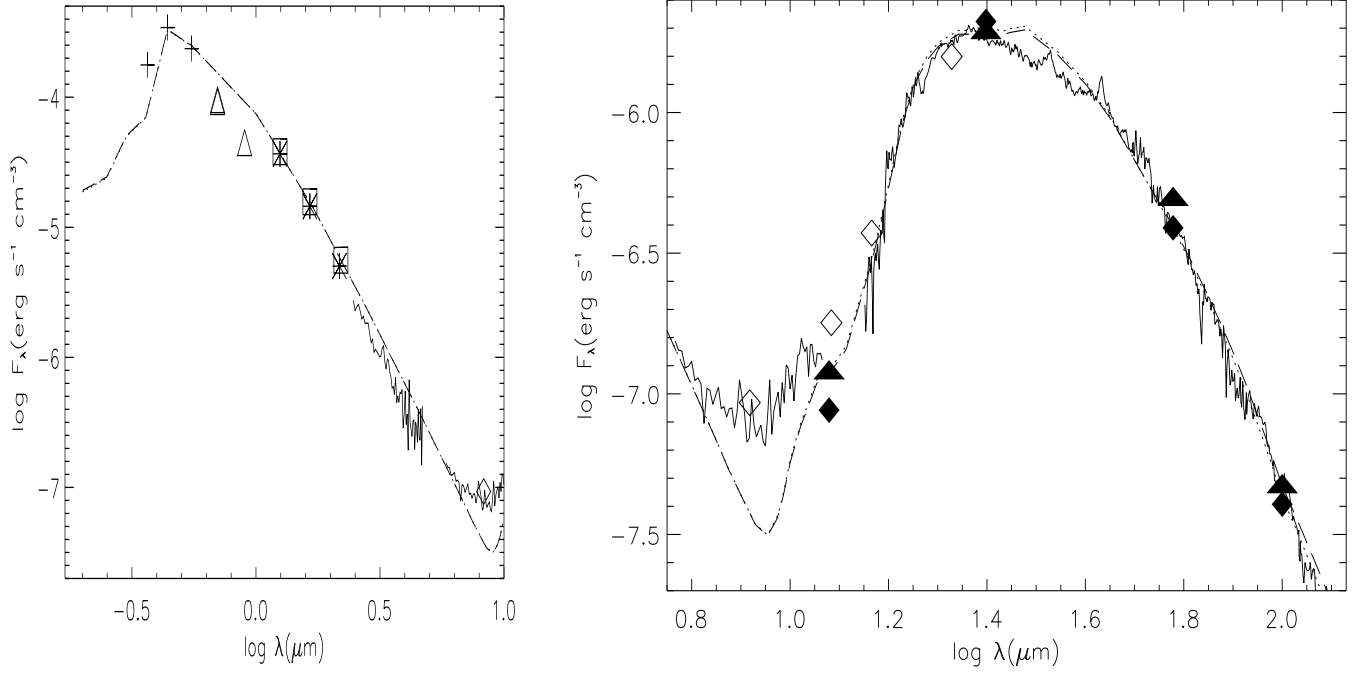


Fig. 7.— As in Fig. 5, but showing model fits using a  $r^{-3}$  density distribution and relative shell thickness of 5 (dotted) and 15 (dashed) (model numbers 7 and 8 in Table 5).

#### 4.4.3. Additional constraints on the models

Recent HST images of I 19475 (Sahai et al. 2006) show a  $r^{-3}$  halo with an inner radius of  $\sim 1.5''$ ; the surface-brightness limited value of the outer radius is  $\sim 5''$ . For our assumed distance (4.9 kpc), these values correspond to  $R_{\text{in}} = 1.1 \times 10^{17} \text{cm}$  and  $R_{\text{out}} = 3.6 \times 10^{17} \text{cm}$ , which are in good agreement with our model values – e.g., in Model 7,  $R_{\text{in}} = 8.8 \times 10^{16} \text{cm}$  and  $R_{\text{out}} = 4.4 \times 10^{17} \text{cm}$ .

Additional constraints on our model are provided by the observed flux of I 19475 at sub-mm wavelengths. Gledhill et al. (2002) measured a flux density of  $34 \pm 5.4 \text{ mJy}$  at  $850 \mu\text{m}$  using a beamwidth of  $13''$ . The wide-band filter used by Gledhill et al. (2002) includes the CO J=3–2 line in its range. However, we find, using formulae from Seaquist et al. (2004) for calculating the line contribution to the filter, and an estimate of the CO J=3–2 line flux from a multi-transition model fit to CO data on I 19475, that the line emission is not likely to contribute more than 20-30% of the observed flux (Sahai et al. 2006). Hence the sub-mm flux of I 19475 is  $\gtrsim 20 \text{ mJy}$ . For our best-fit model (Model 7 with  $r^{-3}$  power law and  $Y=5$ ) we integrated the model surface brightness distribution (in  $\text{Jy arcsec}^{-2}$ ) at  $850 \mu\text{m}$  output by DUSTY, using a  $13''$  diameter aperture to obtain the  $850 \mu\text{m}$  model flux density. DUSTY outputs the surface brightness distribution as a function of normalized (in units of  $R_{\text{in}}$ ) radial distance from the central source. The radial distances were converted into angular radii ( $\theta$ ) using our adopted distance of 4.9 kpc to the source. Thus  $Y=5$  corresponds to a shell size of  $12''$ , for which we find a  $850 \mu\text{m}$  flux density of  $10 \text{ mJy}$ , significantly lower than the observed value. We discuss the implications of this discrepancy for our modelling results in § 5.

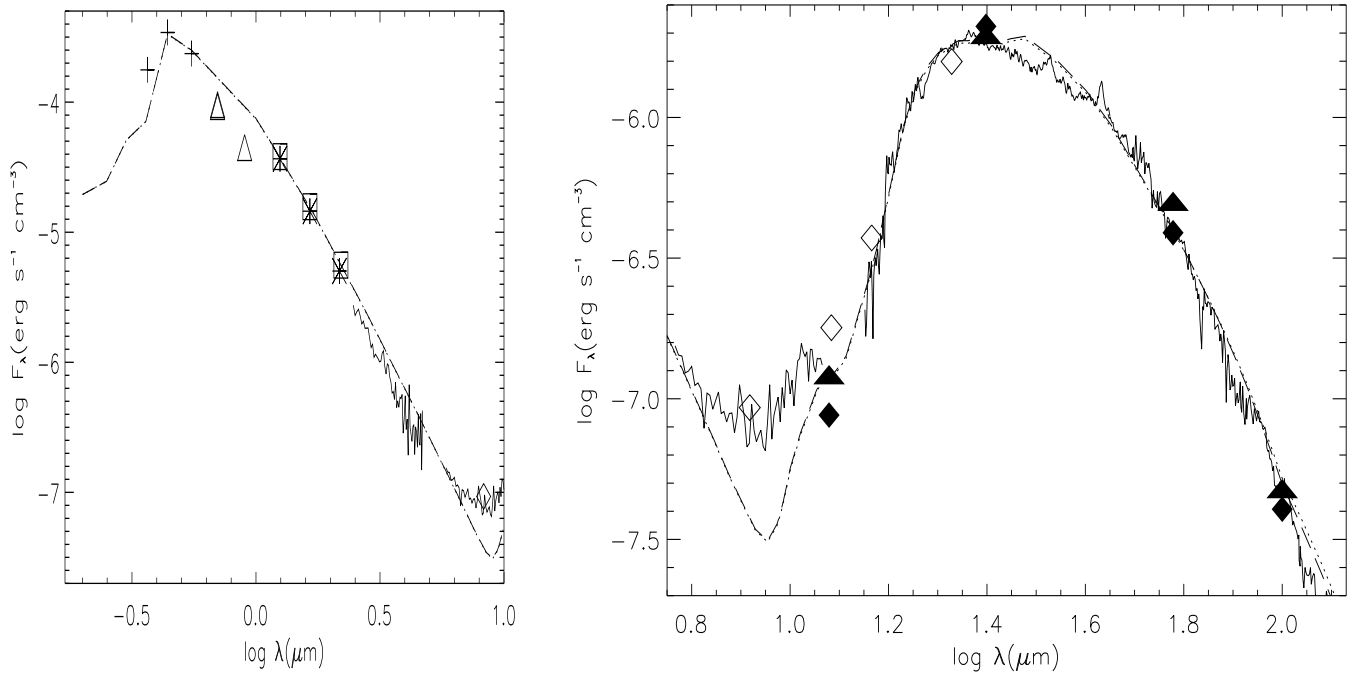


Fig. 8.— As in Fig. 5, but showing model fits with an inner shell of relative thickness 5, and an outer shell of relative thickness 15 (dashed) and 30 (dotted) (model numbers 9 and 10 in Table 5).

#### 4.4.4. Dust shell mass

The mass in the circumstellar dust shell ( $M_s$ ) was computed for each of the models (Table 5). For an  $r^{-3}$  power law dust density law,

$$M_s = 8\pi R_{\text{in}}^2 (1 - Y^{-2})^{-1} \ln Y (\tau_{100}/\kappa_{100}) \delta, \quad (1)$$

where,  $R_{\text{in}}$  is the inner radius of the dust shell (Table 5),  $Y$  is the relative shell thickness ( $R_{\text{out}}/R_{\text{in}}$ ),  $\tau_{100}$  is the shell optical depth at 100  $\mu\text{m}$ ,  $\kappa_{100}$  is the dust mass absorption coefficient at 100  $\mu\text{m}$ , and  $\delta$  is the gas-to-dust ratio. When the density distribution follows a  $r^{-2}$  power law,

$$M_s = 4\pi R_{\text{in}}^2 Y (\tau_{100}/\kappa_{100}) \delta. \quad (2)$$

For the models with an  $r^{-3}$  inner shell, and an  $r^{-2}$  outer shell (see § 5),

$$M_s = 4\pi R_{\text{in}}^2 (\tau_{100}/\kappa_{100}) \delta [\ln Y1 + (Y2/Y1 - 1)]/g(Y1, Y2), \quad (3)$$

where  $g(Y1, Y2) = (1 - 1/Y1^2)/2 + (1 - Y1/Y2)/Y1^2$ , and  $Y1$  and  $Y2$  are the relative shell thicknesses of the inner and outer shell, respectively. The value of the dust mass absorption coefficient  $\kappa$  at far-infrared wavelength is poorly known (e.g. Jura 1986). We use  $\kappa_{100} = 34 \text{ cm}^2 \text{ gm}^{-1}$ , appropriate for the silicate dust used in our models (e.g. tabulated values by Ossenkopf at <http://hera.ph1.uni-koeln.de/~ossk/Jena/tables.html>), and  $\delta=200$  (a typical value for the ejecta from AGB stars) to derive a shell mass of  $1 M_{\odot}$  for our best-fit model (shell masses for this model and others are given in Table 5). The corresponding mass-loss rate is  $3.4 \times 10^{-4} M_{\odot} \text{ yr}^{-1}$  ( $6.7 \times 10^{-5} M_{\odot} \text{ yr}^{-1}$ ) at the inner (outer) radius of the shell, assuming a constant expansion velocity of 16  $\text{km s}^{-1}$  based on CO line observations (Sahai et al. 2006).

Our derived shell mass should really be considered a lower limit because the model SED is not very sensitive to cooler dust at large radii. This is demonstrated by the fact that the quality of the fits to the SED from the additional models with much larger outer radii compared to Model 7 (listed in Table 5), although poorer than the latter, is not drastically worse.

## 5. Discussion

Our model fits to the SED of I 19475 covering the optical to the far-infrared wavelength range are reasonably satisfactory. The radial density distribution and physical size of the dust shell are also in reasonable agreement with the imaging data from HST. Since modelling

of CO J=4-3 and J=2-1 line emission from I 19475 also suggests a  $r^{-3}$  radial-density shell (Hrivnak & Bieging 2005), the  $r^{-3}$  density law for I 19475’s dusty, molecular envelope has strong support. The exponent of the density law characterising the ambient circumstellar medium has important implications for the primary process which results in the observed shapes of PPNs and PNs (Sahai & Trauger 1998) – namely, the interaction of fast collimated post-AGB wind with this medium. For example, the forward shock produced by a fast wind expanding into an  $r^{-2}$  medium moves at constant velocity, but in an  $r^{-3}$  medium, the shock accelerates and is thus subject to Rayleigh-Taylor instabilities. Thus, the dynamical age and the morphology of the lobes in PPNs and PNs are expected to be closely related to the steepness of the radial density power-law distribution.

We note however that there is a caveat to the agreement in the density law exponent between our dust model and the CO models – the latter give a mass-loss rate of  $5.2 \times 10^{-5} M_{\odot} \text{ yr}^{-1}$  at an inner radius  $R_{\text{in}} = 3.9 \times 10^{16} \text{ cm}$  based on (unpublished) mid-infrared imaging data, which is significantly lower than our estimate at an even larger value of  $R_{\text{in}}$ . Since the CO models for inferring the mass-loss rate depend on a number of poorly-known quantities such as the radial kinetic temperature distribution, the inner and outer radius of the CO envelope, and the fractional CO abundance, we believe that our modelling of the dust emission provide an independent and probably more robust estimate of the shell mass and mass-loss rate.

The discrepancy between the observed and model sub-mm flux is intriguing, suggesting that there are either (1) significant quantities of cooler grains in I 19475 than included in our model, and/or (2) the dust emissivity at sub-millimeter wavelengths is significantly larger than the value computed by DUSTY for our assumed grain type and size range. Because the sub-mm observations are rather insensitive to emission at radii beyond the half-power point of their  $13''$  beam, extending our  $12''$  diameter shell to larger sizes does not significantly enhance the model  $850 \mu\text{m}$  flux, and so does not help in resolving the problem of the sub-mm excess. We find this expectation is supported from the results of new models in which we have added an  $r^{-2}$  envelope surrounding the  $r^{-3}$  density distribution in Model 7. We do not find any significant increase in the sub-mm wave flux density for models with relative thicknesses of 15 and 30 for the outer shell (Fig. 8); moreover, in these cases the far-infrared modelled flux begins to exceed the observed flux.

It is rather unlikely that the excess sub-mm flux can be explained by the presence of small grains at radii inside of the half-power point of the millimeter-wave beam, which are sufficiently cool (i.e., for providing the excess observed submillimeter-wave flux) because they are located in regions shielded from the direct stellar radiation. Such regions with significantly higher-than-average extinction could plausibly exist in a 3-D physical model

of I 19475. However, the fundamental difficulty with such a hypothesis is that, since small grains are such poor emitters at sub-millimeter wavelengths, a very large mass of these grains is required to produce the observed submillimeter emission – and such a mass contributes substantially at far-infrared wavelengths (i.e.,  $\sim 100 \mu\text{m}$ ) for which the warm, small grains in our model already produce adequate emission. For example,  $0.01(20 \text{ K}/T_d)M_\odot$  of cold dust at temperature  $T_d$  would be needed to produce the "excess"  $850 \mu\text{m}$  flux of 20 mJy, assuming  $\kappa_{850} \sim 3 \text{ cm}^2 \text{ gm}^{-1}$  (appropriate for small grains; Jura, Webb & Kahane 2001), but this dust contributes far too much emission at far-infrared wavelengths (e.g.  $\sim 20 \text{ Jy}$  at  $100 \mu\text{m}$ ) to be consistent with the data.

Although the nebula clearly has non-spherical components, simply incorporating these by using a 3-D model, but without the addition of large, cooler, dust grains, will not help resolve the problem of the sub-mm excess. We conclude that it is likely that there are much larger dust grains present within our model dust shell which are not accounted for by our adopted dust grain distribution (which follows the standard MRN prescription). Multi-wavelength observations of I 19475's continuum flux at radio, millimeter and sub-millimeter wavelengths will be needed in order to probe the mass and sizes of these grains, and justify further quantitative modelling with modified dust grain properties. High spatial resolution submillimeter-wave interferometric observations with a facility like the Submillimeter Array could help us identify the location of these large, cool grains. One possibility is that the cool grains are associated with the more compact ( $\sim 5''$ ) lobe-pair of this quadrupolar nebula as seen in the HST image (Sahai 2004, Fig. 1).

Gledhill et al. (2002) analysed their  $850 \mu\text{m}$  data of I 19475 (and other sources), together with the  $100 \mu\text{m}$  flux, assuming a fixed dust temperature of 120 K. Although their data provide a potentially important constraint for determining the dust content and mass in PPNs, their analysis and its results (dust mass, dust emissivity power-law index) are most likely invalid because we find from our modelling that the dust temperatures are much lower, and cover a large range (46-94 K). Gledhill et al.'s derived dust mass, scaled to our adopted distance and multiplied by our adopted gas-to-dust ratio, is  $0.7M_\odot$ —that this number is not too different from our estimate of  $\gtrsim 1M_\odot$ , is purely coincidental. Our modelling underscores the importance of first determining the mass and temperature distribution of dust in PPNs carefully by fitting their full near-to-far infrared SEDs, before inferring dust masses from longer-wavelength data.

There are two other wavelength regions where the modelled flux is discrepant from the data. First, in the  $\sim (7 - 11)\mu\text{m}$  range, the model flux is lower than the observed PHT-S data. In this wavelength region, the SED is at a minimum because both the stellar and the dust shell contributions are rapidly declining at wavelengths approaching this region. It is



likely that the observed excess flux in this region results from the presence of a small amount of warm dust (i.e. at temperatures larger than those in our model dust shell – e.g, 94–46 K in the best-fit model), and thus at radii smaller than the inner radius of the cool dust shell. Second, in the  $\sim (27 - 42)\mu\text{m}$  range, the model flux is larger than observed, suggesting a small excess of dust in our model shell at some intermediate temperature range within the full range of temperatures in our model shell. As we have discussed in Sec. 3.1, we believe that amorphous water-ice is not a significant contributor in this region and therefore it is unlikely to help in removing this discrepancy. Both discrepancies are probably best addressed by going to a 2-D model of the object.

### 5.1. Modelling Uncertainties

From the off-source LWS spectrum (Fig. 2b), it is obvious that there is an increasing and substantial amount of background contribution to the LWS source data (Fig. 2a) beyond  $90\mu\text{m}$ . Although considerable care was taken in subtracting the background spectrum from the source spectrum (Fig. 2c), this remains a possible source of uncertainty in our modelling – however, we do not think it affects our major conclusions. The need to adopt an  $r^{-3}$  (rather than a  $r^{-2}$ ) density law is driven by a *systematic* excess in the model flux above the observed flux over a large wavelength range, i.e. for all wavelengths longwards of  $\sim 70\mu\text{m}$  (§4.4.2). This excess cannot be purely a result of the uncertainty in the background correction, since the total background correction upto  $90\mu\text{m}$  is less than  $\sim 10\%$ , with the uncertainty in the correction being significantly smaller. The submillimeter excess which we find in I 19475 is also too large to be accounted for by uncertainties in the LWS background subtraction.

We would like to point out that in this paper, the emphasis in the fitting procedure is not on the details of the mineralogy of the dust, but rather on the bulk dust component which is comprised of amorphous silicates. Given that we do not have a convincing detection of water-ice in the dust in I 19475, a detailed investigation of models with amorphous water-ice (e.g., its affect on the observed  $43\mu\text{m}$  emission feature and the overall spectral shape) does not appear warranted.

## 6. Conclusions

We have reconstructed the spectral energy distribution of the pre-planetary nebula IRAS 19475+3119, from the optical to the far-infrared, using ISO spectra and broad-band photometric data. Features at  $33.6\mu\text{m}$ ,  $43\mu\text{m}$ , and possibly at  $23\mu\text{m}$ , identified in the ISO

SWS spectrum of the star, are most likely due to the presence of crystalline silicates.

The circumstellar dust envelope of the star was modelled using the 1-D radiative transfer code, DUSTY. We find that the dust shell has a very substantial mass, of  $\gtrsim 1M_{\odot}$ , in all models which provide a reasonable fit to the data. Our best fit is obtained for a shell with an  $r^{-3}$  radial density, inner and outer radii of  $8.8 \times 10^{16}$  and  $4.4 \times 10^{17}$  cm, dust temperatures ranging from about 94 K to 46 K, and  $\tau(0.55 \mu\text{m})=1$ . The mass of this shell is  $\gtrsim 1 [34 \text{ cm}^2 \text{ g}^{-1} / \kappa(100 \mu\text{m})][\delta/200]M_{\odot}$ , where  $\kappa(100 \mu\text{m})$  is the  $100 \mu\text{m}$  dust mass absorption coefficient (per unit dust mass), and  $\delta$  is the gas-to-dust ratio.

In agreement with results from optical imaging and millimeter-wave observations of CO emission, our model fits support an  $r^{-3}$  density law for I 19475's dust shell. The exponent of the density law characterising the ambient circumstellar medium has important implications for the interaction process between the fast collimated post-AGB winds and the dense AGB envelopes which results in the observed shapes of PPNs and PNs.

Our models show some discrepancies with the data. The most significant of these is that the observed JCMT flux at sub-millimeter wavelengths ( $850 \mu\text{m}$ ) is a factor  $\sim 2$  larger than the model flux, suggesting the presence of dust grains in the dust shell of I 19475 which are significantly larger than those accounted for by our adopted model dust grain distribution.

RS is thankful to NASA for financial support for this study from the Astrophysics Data Program (RTOP 399-20-00-08), and from the Space Telescope Science Institute through Program number HST-GO-09463.01.

Table 5: Input and output parameters for DUSTY model fits to the observed data

Model number	Grain type	Density law	$T_d$ (K)	$\tau$		$R_{in}^\dagger$ (cm)	Shell thickness	Shell Mass ( $M_\odot$ )
				at $0.55 \mu m$	at $100 \mu m$			
1	Sil-Ow	$r^{-3}$	95	1.00	$9.874 \times 10^{-4}$	$8.54 \times 10^{16}$	10	1.24
2	Sil-Oc	$r^{-3}$	88	1.00	$8.404 \times 10^{-4}$	$1.00 \times 10^{17}$	10	1.45
3	Sil-DL	$r^{-3}$	93	1.50	$2.631 \times 10^{-3}$	$5.70 \times 10^{16}$	10	1.47
4	Sil-Ow	$r^{-2}$	96	1.05	$1.037 \times 10^{-3}$	$8.06 \times 10^{16}$	5	1.25
5	Sil-Ow	$r^{-2}$	100	1.10	$1.086 \times 10^{-3}$	$7.12 \times 10^{16}$	10	2.05
6	Sil-Ow	$r^{-2}$	102	1.10	$1.086 \times 10^{-3}$	$6.71 \times 10^{16}$	15	2.72
7	Sil-Ow	$r^{-3}$	94	1.00	$9.874 \times 10^{-4}$	$8.84 \times 10^{16}$	5	0.96
8	Sil-Ow	$r^{-3}$	94	1.00	$9.874 \times 10^{-4}$	$8.80 \times 10^{16}$	15	1.54
9	Sil-Ow	$r^{-3}, r^{-2}$	94	1.00	$9.874 \times 10^{-4}$	$8.77 \times 10^{16}$	5, 15	2.01
10	Sil-Ow	$r^{-3}, r^{-2}$	94	1.00	$9.874 \times 10^{-4}$	$8.76 \times 10^{16}$	5, 30	3.63

$^\dagger$ : The inner radius of the dust shell where the dust temperature ( $T_d$ ) is specified.  $R_{in}$  as output by DUSTY scales as  $L^{1/2}$  where,  $L$  is the luminosity. The  $R_{in}$  values listed here are for a central star luminosity of  $8300 L_\odot$ .

## A. Data reduction

Offline processed SWS (OLP version 10.1), LWS (OLP version 10.0) and PHT-S (OLP version 10.0) data were retrieved from the ISO data archive. The SWS and LWS observations were further processed using ISAP (ISO Spectroscopic Analysis Package) version 2.1.

### A.1. SWS

The data analysis using ISAP consisted of extensive bad data removal primarily to minimize the effect of cosmic ray hits. All detectors were compared to identify possible features. For each sub-band, ‘offset’ shifts were applied to bring the flux level of the 12 detectors to a mean value (Sturm 2000). The spectra of the 12 detectors were then averaged using median clipping to discard points that lay more than  $2.5\sigma$  from the median flux. The averaging was done to a resolution of 300 and 1500 for SWS01 data taken with speed 1 and 4 respectively (Table 1). The data of sub-band 3E(27.5–29.0  $\mu\text{m}$ ) are generally noisy and unreliable (see e.g. Hrivnak et al. 2000; Hony et al. 2002). Our SWS data, below band 3A (16.5  $\mu\text{m}$ ) is very noisy. This is also evident from the low IRAS flux at 12  $\mu\text{m}$  (0.54 Jy). The averaged spectra of sub-band 3D (19.5–27.5  $\mu\text{m}$ ) were scaled in order to match the flux at 25  $\mu\text{m}$  with the observed IRAS flux at this wavelength. Appropriate scaling factors were then applied to the remaining sub-bands in order to form a continuous spectrum from 2.38–45.2  $\mu\text{m}$ .

### A.2. LWS

Reduction of the LWS on and off-source observations consisted of extensive bad data removal using ISAP and rebinning on a fixed resolution grid of  $\lambda/\Delta\lambda = 250$ . In the case of the on-source data, for each detector, we examined the OLP dark current estimates made before (Dark 0) and after (Dark 1) the observation using LWS Interactive Analysis (LIA) version 10.2. To form a continuous spectrum from 43–197  $\mu\text{m}$ , using ISAP\_SHIFT routine, we applied a ‘DC offset’ shift to the detectors which showed different Dark 0 and Dark 1 values. Dark current measurements of detectors LW3 (123–152  $\mu\text{m}$ ), LW4 (142–171  $\mu\text{m}$ ) and LW5 (161–197  $\mu\text{m}$ ) showed a decreasing temporal shift. Hence a ‘gain’ correction was applied to these 3 detectors using the ISAP\_SHIFT routine (Molinari) to match the flux in the overlapping spectral regions between the detectors.

The background spectrum was rebinned to the same wavelength scale as the source spectrum. It was assumed that the [C II] emission at 158  $\mu\text{m}$  in the on-source spectrum is

entirely interstellar in origin. The background spectrum was therefore scaled in the region of the [C II] line (LW4 detector) to match the line strength in the on and off-source data. Then, using the LW4 detector as a reference the remaining detectors were scaled to form a continuous off-source spectrum (Fig. 2b). Subsequently, the LWS spectrum of I19475 (Fig. 2c) was obtained by subtracting the off-source spectrum (Fig. 2b) from the on-source data (Fig. 2a).

### A.3. PHT-S

The fully processed PHT-S data of I19475 retrieved from the ISO data archive is scientifically validated and was used directly (i.e. with no further processing). The typical calibration accuracy for PHT-S observations made in staring, extended source mode is better than  $\pm 15\%$  (Klaas et al., 2002). The PHT-S data,  $I_\lambda(i)$  in units of surface brightness ( $\text{W m}^{-2} \mu\text{m}^{-1} \text{sr}^{-1}$ ) obtained from the archive was converted to flux density,  $F_\lambda(i)$  units ( $\text{W m}^{-2} \mu\text{m}^{-1}$ ) using the recipe given in Laureijs et al. (2003) :

$$F_\lambda(i) = 10^{-6} I_\lambda(i) \frac{C_{ave}^e}{C_{ave}^p}$$

where,

- $I_\lambda(i)$  in  $\text{W m}^{-2} \mu\text{m}^{-1} \text{sr}^{-1}$  is the surface brightness for a given detector array element  $i$ ;
- $\lambda(i)$  in  $\mu\text{m}$  is the central wavelength of a PHT-S detector pixel;
- $C_{ave}^e(i)$  in  $(\text{Vs}^{-1})/(\text{MJysr}^{-1})$  is the average spectral response function for the conversion from signal in  $\text{Vs}^{-1}$  to surface brightness in  $\text{MJysr}^{-1}$ ;
- $C_{ave}^p(i)$  in  $(\text{Vs}^{-1})/\text{Jy}$  is the average spectral response function for the conversion from signal in  $(\text{Vs}^{-1})$  to point source flux density in Jy.

The conversion factors  $C_{ave}^e$  and  $C_{ave}^p$  (Table 6) were obtained from the PSPECAL.FITS file which is part of the general calibration files (Cal-G) distributed with the ISOPHOT Interactive Analysis (PIA), version 10.0.

Table 6: Conversion factors for PHT-S data

Wavelength ( $\mu\text{m}$ )	$C_{ave}^e(i)$ ( $\text{Vs}^{-1}$ )/(MJysr $^{-1}$ )	$C_{ave}^p(i)$ ( $\text{Vs}^{-1}$ )/Jy	$\frac{C_{ave}^e(i)}{C_{ave}^p(i)}$ Jy/(MJysr $^{-1}$ )
2.46870	$3.03987 \times 10^{-5}$	0.00333517	$9.11459 \times 10^{-3}$
2.50950	$3.01950 \times 10^{-5}$	0.00328285	$9.19780 \times 10^{-3}$
2.55010	$3.23561 \times 10^{-5}$	0.00348378	$9.28764 \times 10^{-3}$
2.59070	$3.14137 \times 10^{-5}$	0.00335591	$9.36071 \times 10^{-3}$
2.63110	$3.55078 \times 10^{-5}$	0.00376118	$9.44060 \times 10^{-3}$
2.67150	$3.47183 \times 10^{-5}$	0.00364872	$9.51520 \times 10^{-3}$
2.71180	$3.33576 \times 10^{-5}$	0.00348496	$9.57187 \times 10^{-3}$
2.75210	$3.41233 \times 10^{-5}$	0.00354108	$9.63641 \times 10^{-3}$
2.79220	$3.62736 \times 10^{-5}$	0.00374119	$9.69574 \times 10^{-3}$
2.83230	$3.82493 \times 10^{-5}$	0.00391801	$9.76243 \times 10^{-3}$
2.87220	$4.02213 \times 10^{-5}$	0.00409953	$9.81120 \times 10^{-3}$
2.91210	$3.68381 \times 10^{-5}$	0.00373792	$9.85524 \times 10^{-3}$
2.95190	$4.81234 \times 10^{-5}$	0.00485787	$9.90628 \times 10^{-3}$
2.99170	$5.82109 \times 10^{-5}$	0.00585568	$9.94093 \times 10^{-3}$
3.03130	$7.06671 \times 10^{-5}$	0.00708768	$9.97041 \times 10^{-3}$
3.07090	$6.49100 \times 10^{-5}$	0.00648637	$1.00071 \times 10^{-2}$
3.11030	$6.87588 \times 10^{-5}$	0.00684926	$1.00389 \times 10^{-2}$
3.14970	$6.13806 \times 10^{-5}$	0.00610456	$1.00549 \times 10^{-2}$
3.18900	$7.19383 \times 10^{-5}$	0.00713846	$1.00776 \times 10^{-2}$
3.22830	$6.93928 \times 10^{-5}$	0.00687342	$1.00958 \times 10^{-2}$
3.26740	$7.03575 \times 10^{-5}$	0.00695950	$1.01096 \times 10^{-2}$
3.30650	$6.28810 \times 10^{-5}$	0.00621426	$1.01188 \times 10^{-2}$
3.34550	$6.44410 \times 10^{-5}$	0.00636565	$1.01232 \times 10^{-2}$
3.38430	$5.97321 \times 10^{-5}$	0.00590055	$1.01231 \times 10^{-2}$
3.42320	$6.31887 \times 10^{-5}$	0.00624471	$1.01188 \times 10^{-2}$
3.46190	$5.41975 \times 10^{-5}$	0.00536089	$1.01098 \times 10^{-2}$
3.50050	$5.34569 \times 10^{-5}$	0.00529456	$1.00966 \times 10^{-2}$

Table 6: contd....

Wavelength ( $\mu\text{m}$ )	$C_{ave}^e(i)$ ( $\text{Vs}^{-1}$ )/( $\text{MJysr}^{-1}$ )	$C_{ave}^p(i)$ ( $\text{Vs}^{-1}$ )/Jy	$\frac{C_{ave}^e(i)}{C_{ave}^p(i)}$ Jy/( $\text{MJysr}^{-1}$ )
3.53910	$4.24939 \times 10^{-5}$	0.00421167	$1.00896 \times 10^{-2}$
3.57760	$5.09418 \times 10^{-5}$	0.00506002	$1.00675 \times 10^{-2}$
3.61600	$4.31928 \times 10^{-5}$	0.00430166	$1.00410 \times 10^{-2}$
3.65430	$3.78045 \times 10^{-5}$	0.00377251	$1.00210 \times 10^{-2}$
3.69250	$2.49969 \times 10^{-5}$	0.00250331	$9.98554 \times 10^{-3}$
3.73070	$3.35651 \times 10^{-5}$	0.00329863	$1.01755 \times 10^{-2}$
3.76870	$3.71818 \times 10^{-5}$	0.00364488	$1.02011 \times 10^{-2}$
3.80670	$3.82232 \times 10^{-5}$	0.00373432	$1.02357 \times 10^{-2}$
3.84460	$3.29000 \times 10^{-5}$	0.00320791	$1.02559 \times 10^{-2}$
3.88240	$3.63065 \times 10^{-5}$	0.00352998	$1.02852 \times 10^{-2}$
3.92010	$3.44827 \times 10^{-5}$	0.00334782	$1.03000 \times 10^{-2}$
3.95780	$3.76135 \times 10^{-5}$	0.00364328	$1.03241 \times 10^{-2}$
3.99540	$3.25984 \times 10^{-5}$	0.00315459	$1.03336 \times 10^{-2}$
4.03280	$3.26180 \times 10^{-5}$	0.00315082	$1.03522 \times 10^{-2}$
4.07020	$2.89407 \times 10^{-5}$	0.00279106	$1.03691 \times 10^{-2}$
4.10760	$3.27721 \times 10^{-5}$	0.00315620	$1.03834 \times 10^{-2}$
4.14480	$2.82243 \times 10^{-5}$	0.00271870	$1.03815 \times 10^{-2}$
4.18190	$3.10457 \times 10^{-5}$	0.00298790	$1.03905 \times 10^{-2}$
4.21900	$2.72054 \times 10^{-5}$	0.00261666	$1.03970 \times 10^{-2}$
4.25600	$2.69869 \times 10^{-5}$	0.00259448	$1.04017 \times 10^{-2}$
4.29290	$2.27141 \times 10^{-5}$	0.00218314	$1.04043 \times 10^{-2}$
4.32970	$2.39768 \times 10^{-5}$	0.00230451	$1.04043 \times 10^{-2}$
4.36640	$2.07467 \times 10^{-5}$	0.00199824	$1.03825 \times 10^{-2}$
4.40310	$2.35388 \times 10^{-5}$	0.00226821	$1.03777 \times 10^{-2}$
4.43970	$1.94929 \times 10^{-5}$	0.00187972	$1.03701 \times 10^{-2}$
4.47610	$2.18277 \times 10^{-5}$	0.00210694	$1.03599 \times 10^{-2}$
4.51250	$1.81484 \times 10^{-5}$	0.00175392	$1.03473 \times 10^{-2}$

Table 6: contd....

Wavelength ( $\mu\text{m}$ )	$C_{ave}^e(i)$ ( $\text{Vs}^{-1}$ )/( $\text{MJysr}^{-1}$ )	$C_{ave}^p(i)$ ( $\text{Vs}^{-1}$ )/Jy	$\frac{C_{ave}^e(i)}{C_{ave}^p(i)}$ Jy/( $\text{MJysr}^{-1}$ )
4.54890	$1.98181 \times 10^{-5}$	0.00191809	$1.03322 \times 10^{-2}$
4.58510	$1.62796 \times 10^{-5}$	0.00157838	$1.03141 \times 10^{-2}$
4.62120	$1.42384 \times 10^{-5}$	0.00138326	$1.02934 \times 10^{-2}$
4.65730	$1.44786 \times 10^{-5}$	0.00140976	$1.02703 \times 10^{-2}$
4.69330	$1.50828 \times 10^{-5}$	0.00147225	$1.02447 \times 10^{-2}$
4.72920	$1.36050 \times 10^{-5}$	0.00132851	$1.02408 \times 10^{-2}$
4.76500	$1.80055 \times 10^{-5}$	0.00176359	$1.02096 \times 10^{-2}$
4.80080	$1.34228 \times 10^{-5}$	0.00131913	$1.01755 \times 10^{-2}$
4.83640	$1.44308 \times 10^{-5}$	0.00142338	$1.01384 \times 10^{-2}$
5.83960	$12.8575 \times 10^{-5}$	0.0115198	$1.11612 \times 10^{-2}$
5.93380	$11.4284 \times 10^{-5}$	0.0102716	$1.11262 \times 10^{-2}$
6.02800	$11.2309 \times 10^{-5}$	0.0100773	$1.11448 \times 10^{-2}$
6.12200	$11.6475 \times 10^{-5}$	0.0104899	$1.11035 \times 10^{-2}$
6.21600	$10.9303 \times 10^{-5}$	0.00983196	$1.11171 \times 10^{-2}$
6.30990	$8.64221 \times 10^{-5}$	0.00776619	$1.11280 \times 10^{-2}$
6.40380	$10.6843 \times 10^{-5}$	0.00964404	$1.10787 \times 10^{-2}$
6.49750	$9.88445 \times 10^{-5}$	0.00891797	$1.10837 \times 10^{-2}$
6.59120	$9.40491 \times 10^{-5}$	0.00848214	$1.10879 \times 10^{-2}$
6.68480	$8.12382 \times 10^{-5}$	0.00732521	$1.10902 \times 10^{-2}$
6.77830	$9.59879 \times 10^{-5}$	0.00870225	$1.10302 \times 10^{-2}$
6.87170	$9.17306 \times 10^{-5}$	0.00831815	$1.10278 \times 10^{-2}$
6.96500	$10.4062 \times 10^{-5}$	0.00944026	$1.10232 \times 10^{-2}$
7.05830	$9.92587 \times 10^{-5}$	0.00900942	$1.10172 \times 10^{-2}$
7.15150	$9.66050 \times 10^{-5}$	0.00877220	$1.10126 \times 10^{-2}$
7.24460	$8.08621 \times 10^{-5}$	0.00734715	$1.10059 \times 10^{-2}$
7.33760	$7.66112 \times 10^{-5}$	0.00696665	$1.09968 \times 10^{-2}$
7.43060	$6.90864 \times 10^{-5}$	0.00628884	$1.09856 \times 10^{-2}$



Table 6: contd....

Wavelength ( $\mu\text{m}$ )	$C_{ave}^e(i)$ ( $\text{Vs}^{-1}$ )/(MJysr $^{-1}$ )	$C_{ave}^p(i)$ ( $\text{Vs}^{-1}$ )/Jy	$\frac{C_{ave}^e(i)}{C_{ave}^p(i)}$ Jy/(MJysr $^{-1}$ )
7.52350	$8.15585 \times 10^{-5}$	0.00743328	$1.09721 \times 10^{-2}$
7.61630	$7.35407 \times 10^{-5}$	0.00671185	$1.09568 \times 10^{-2}$
7.70900	$7.07851 \times 10^{-5}$	0.00647062	$1.09395 \times 10^{-2}$
7.80160	$6.83308 \times 10^{-5}$	0.00625740	$1.09200 \times 10^{-2}$
7.89420	$7.86450 \times 10^{-5}$	0.00716019	$1.09836 \times 10^{-2}$
7.98660	$7.69969 \times 10^{-5}$	0.00702496	$1.09605 \times 10^{-2}$
8.07900	$7.75643 \times 10^{-5}$	0.00709291	$1.09355 \times 10^{-2}$
8.17140	$6.57546 \times 10^{-5}$	0.00602763	$1.09089 \times 10^{-2}$
8.26360	$6.08753 \times 10^{-5}$	0.00559467	$1.08809 \times 10^{-2}$
8.35580	$5.63152 \times 10^{-5}$	0.00514833	$1.09385 \times 10^{-2}$
8.44780	$6.16770 \times 10^{-5}$	0.00565487	$1.09069 \times 10^{-2}$
8.53980	$5.88137 \times 10^{-5}$	0.00540839	$1.08745 \times 10^{-2}$
8.63180	$6.33101 \times 10^{-5}$	0.00583982	$1.08411 \times 10^{-2}$
8.72360	$3.26216 \times 10^{-5}$	0.00299513	$1.08915 \times 10^{-2}$
8.81540	$5.01120 \times 10^{-5}$	0.00490196	$1.02228 \times 10^{-2}$
8.90700	$5.79664 \times 10^{-5}$	0.00562173	$1.03111 \times 10^{-2}$
8.99860	$5.44365 \times 10^{-5}$	0.00519205	$1.04846 \times 10^{-2}$
9.09020	$5.10184 \times 10^{-5}$	0.00483174	$1.05590 \times 10^{-2}$
9.18160	$4.59752 \times 10^{-5}$	0.00428244	$1.07357 \times 10^{-2}$
9.27300	$4.28071 \times 10^{-5}$	0.00396460	$1.07973 \times 10^{-2}$
9.36430	$4.05319 \times 10^{-5}$	0.00373380	$1.08554 \times 10^{-2}$
9.45550	$4.54677 \times 10^{-5}$	0.00412516	$1.10229 \times 10^{-2}$
9.54660	$4.58967 \times 10^{-5}$	0.00414712	$1.10671 \times 10^{-2}$
9.63760	$3.91220 \times 10^{-5}$	0.00348406	$1.12289 \times 10^{-2}$
9.72860	$3.55302 \times 10^{-5}$	0.00315427	$1.12642 \times 10^{-2}$
9.81950	$2.83132 \times 10^{-5}$	0.00247981	$1.14175 \times 10^{-2}$
9.91030	$3.39671 \times 10^{-5}$	0.00296851	$1.14425 \times 10^{-2}$

Table 6: contd....

Wavelength ( $\mu\text{m}$ )	$C_{ave}^e(i)$ ( $\text{Vs}^{-1}$ )/( $\text{MJysr}^{-1}$ )	$C_{ave}^p(i)$ ( $\text{Vs}^{-1}$ )/Jy	$\frac{C_{ave}^e(i)}{C_{ave}^p(i)}$ Jy/( $\text{MJysr}^{-1}$ )
10.0010	$3.34585 \times 10^{-5}$	0.00288679	$1.15902 \times 10^{-2}$
10.0917	$2.71791 \times 10^{-5}$	0.00234248	$1.16027 \times 10^{-2}$
10.1823	$2.93380 \times 10^{-5}$	0.00249772	$1.17459 \times 10^{-2}$
10.2727	$3.21568 \times 10^{-5}$	0.00273768	$1.17460 \times 10^{-2}$
10.3632	$2.83052 \times 10^{-5}$	0.00238194	$1.18833 \times 10^{-2}$
10.4535	$2.61391 \times 10^{-5}$	0.00220172	$1.18721 \times 10^{-2}$
10.5437	$2.52504 \times 10^{-5}$	0.00210409	$1.20006 \times 10^{-2}$
10.6339	$2.60993 \times 10^{-5}$	0.00217871	$1.19792 \times 10^{-2}$
10.7240	$2.67050 \times 10^{-5}$	0.00220733	$1.20983 \times 10^{-2}$
10.8140	$2.50139 \times 10^{-5}$	0.00207279	$1.20677 \times 10^{-2}$
10.9040	$2.50909 \times 10^{-5}$	0.00206055	$1.21768 \times 10^{-2}$
10.9938	$2.42555 \times 10^{-5}$	0.00199853	$1.21367 \times 10^{-2}$
11.0836	$2.15947 \times 10^{-5}$	0.00176475	$1.22367 \times 10^{-2}$
11.1733	$2.05535 \times 10^{-5}$	0.00166620	$1.23356 \times 10^{-2}$
11.2629	$1.76285 \times 10^{-5}$	0.00143567	$1.22789 \times 10^{-2}$
11.3524	$1.74882 \times 10^{-5}$	0.00141409	$1.23671 \times 10^{-2}$
11.4419	$2.05966 \times 10^{-5}$	0.00167428	$1.23018 \times 10^{-2}$
11.5313	$2.31557 \times 10^{-5}$	0.00187026	$1.23810 \times 10^{-2}$
11.6206	$1.98068 \times 10^{-5}$	0.00159024	$1.24552 \times 10^{-2}$

## REFERENCES

- Arellano Ferro, A., Giridhar, S., Mathias, P., 2001, A&A, 368, 250
- Blöcker, T., 1995, A&A, 299, 755
- Castro-Carrizo, A., Fong, D., Bujarrabal, V., et al., 2001, in *The Promise of the Herschel Space Observatory*, eds. G.L. Pilbratt, J. Cernicharo, A.M. Heras, T. Prusti & R. Harris, ESA-SP 460, p. 257
- Clegg, P.E., Ade, P.A.R., Armand, C., et al., 1996, A&A, 315,
- de Graauw, Th., Haser, L. N. Beintema, D. A., et al., 1996, A&A, 315, L49
- Cohen, M., Walker, R.G., Witteborn, F.C., 1992, AJ, 104, 2030
- Dijkstra, C., Waters, L.B.F.M., Kemper, F. et al., 2003a, A&A, 399, 1037
- Dijkstra, C., Dominik, C., Hoogzaad, S.N., de Koter, A., Min, M., 2003, A&A, 401, 599
- Draine, B.T., & Lee, H.M., 1984, ApJ, 285, 89
- Ferrarotti, A., Gail, H.-P., Degiorgi, L. & Ott, H.R., 2000, A&A, 357, L13
- García-Laro, P., Manchado, A., Pych, W., Pottasch, S.R., 1997, A&AS, 126, 479
- Gauba, G. & Parthasarathy, M., 2004, A&A, 417, 201
- Gledhill, T. M., Chrysostomou, A., Hough, J. H., Yates, J. A., 2001, MNRAS, 322, 321
- Gledhill, T. M., Bains, I., and Yates, J. A., 2002, MNRAS, 332, L55
- Hakkila, J., Myers, J.M., Stidham, B.J. & Hartmann, D.H. 1997, AJ, 114, 2043
- Hanner, M.S., 1988, NASA Cong. Pub., 3004, 22
- Hoogzaad, S.N., Molster, F.J., Dominik, C. et al., 2002, A&A, 389, 547
- Hony, S., Waters, L.B.F.M. & Tielens, A.G.G.M., 2002, A&A, 390, 533
- Hrivnak, B.J., Volk, K. & Kwok, S., 2000, ApJ, 535, 275
- Hrivnak, B.J. & Bieging, J.H., 2005, ApJ, 624, 331
- Ivezić, Z., Nenkova, M., Elitzur, M., 1999, *User Manual for DUSTY*, University of Kentucky Internal Report

- Klochkova, V. G., Panchuk, V. E., Tavalzhanskaya, N. S., 2002, *AstL*, 28, 49
- Jura, M. 1986, *ApJ*, 303, 327
- Klaas, U., Acosta-Pulido, J.A., Ábrahám, P., et al., 1997, ISOPHOT-S: CAPABILITIES and CALIBRATION, in *Proc. First ISO Workshop on Analytical Spectroscopy*, ed. A.M. Heras, K. Leech, N. R. Trams & M. Perry (ESA SP-419), 113
- Klaas, U., Ábrahám, P., Laureijs, R.J. et al., 2002, *ISOPHOT Calibration Accuracies, Version 5.0*,  
<http://www.iso.vilspa.esa.es/instr/PHT/>
- Laureijs, R.J., Ulrich, K., Richards, P.J., Schulz, B. & Ábrahám, P., 2003, *The ISO Handbook, Volume IV: PHT - The Imaging Photo-Polarimeter*, SAI-99-069/Dc, Version 2.0.1
- Lee, Chin-Fei, Sahai, R., 2003, *ApJ*, 586, 319
- Lee, Chin-Fei, Sahai, R., 2004, *ApJ*, 606, 483
- Likkel, L., Omont, A., Morris, M., Forveille, T., 1987, *A&A*, 173, L11
- Lim, T., *private communication*
- Loup, C., Forveille, T., Omont, A., Paul, J. F., 1993, *A&AS*, 99, 291
- Mathis, J.S., Rumpl, W. & Nordsieck, K.H., 1977, *ApJ*, 17, 25
- Matsuura, M., Zijlstra, A.A., Molster, F.J., et al., 2004, *ApJ*, 604, 791
- Molinari, S., *Data reduction recipe for an LWS01 AOT. The case of a faint source*  
[http://www.ipac.caltech.edu/iso/lws/lia/lws01\\_faint.html](http://www.ipac.caltech.edu/iso/lws/lia/lws01_faint.html)
- Molster, F.J., Lim, T.L., Sylvester, R.J., et al., 2001, *A&A*, 372, 165
- Molster, F.J., Waters, L.B.F.M., Tielens, A.G.G.M., Barlow, M.J., 2002a, *A&A*, 382, 184
- Molster, F.J., Waters, L.B.F.M., Tielens, A.G.G.M., 2002b, *A&A*, 382, 222
- Molster, F.J., Waters, L.B.F.M., Tielens, A.G.G.M. et al., 2002c, *A&A*, 382, 241
- Monet, D.G., Levine, S.E., Casian, B., et al., 2003, *AJ*, 125, 984
- Omont, A., Loup, C., Forveille, T., et al., 1993, *A&A*, 267, 515

- Ossenkopf, V., Henning, Th. & Mathis, J.S., 1992, A&A, 261, 567
- Parthasarathy, M., Pottasch, S.R., 1986, A&A, 154L, 16
- Pégourié, B., 1988, A&A, 194, 335
- Reed, C., 2001, JRASC, 95, 268
- Rieke, G.H. & Lebofsky, M.J., 1985, ApJ, 288, 618
- Sahai, R., & Trauger, J. T.1998, AJ, 116, 1357
- Sahai, R., 2002, Astr.Sp.Sc.Lib. 265, 53
- Sahai, R., 2004, in Asymetrical Planetary Nebulae III, ASP Conf. Ser. 313, M. Meixner, J. Kastner, B. Balick & N. Soker eds., p.141
- Sahai, R., et al., 2006, in preparation
- Schlegel, D.J., Finkbeiner, D.P., & Davis, M., 1998, ApJ, 500, 525
- Schmidt-Kaler, Th., 1982, in Landolt-Börnstein: Numerical Data and Functional Relationships in Science and Technology, vol. 2b, ed. K. Schaifers & H. H. Voigt (Berlin: Springer-Verlag)
- Seaquist, E., Yao, L., Dunne, L. and Cameron, H. 2004, MNRAS, 349, 1428
- Sivarani, T., Parthasarathy, M., García-Lario, P., Manchado, A., 2001, in *Post-AGB Objects as a Phase of Stellar Evolution* eds., R. Szczerba & S. K. Górny, Astrophysics & Space Science Library, Vol. 265, p. 301
- Smith, R.G., Robinson, G., Hyland, A.R., Carpenter, G.L., 1994, MNRAS, 271, 481
- Stock, J., Nassau, J.J., Stephenson, C.B., 1960, *Luminous Stars in the Northern Milky Way II* (Hamburger Sternwarte and Warner and Swasey Obs.: Hamburg-Bergedorf)
- Sturm, E., 2000, *How to reduce SWS AOT01 data in the ISAP GUI*, ISO Explanatory Library Doc.,  
[http://www.ipac.caltech.edu/iso/sws/new\\_recipes/sws01\\_recipe.ps](http://www.ipac.caltech.edu/iso/sws/new_recipes/sws01_recipe.ps)
- Sylvester, R.J., Kemper, F., Barlow, M.J., et al., 1999, A&A, 352, 587
- Swinyard, B.M., Clegg, P.E., Ade, P.A.R., et al., 1996, A&A, 315, L43
- Ueta, T., Meixner, M., & Bobrowsky, M. 2000, ApJ, 528, 861

Waters, L.B.F.M., Molster, F.J., de Jong, T., et al., 1996, A&A, 315, L361

Waters, L.B.F.M. & Molster, F.J., 1999, IAU Symp., 191, 209, ed. T. Le Bertre, A. Lébre  
& C. Waelkens